Controlled electrochemical growth of ultra-long gold nanoribbons

Gobind Basnet, Krishna R. Panta, Prem S. Thapa, and Bret N. Flanders

Citation: Appl. Phys. Lett. **110**, 073106 (2017); doi: 10.1063/1.4976027
View online: http://dx.doi.org/10.1063/1.4976027
View Table of Contents: http://aip.scitation.org/toc/apl/110/7
Published by the American Institute of Physics

Controlled electrochemical growth of ultra-long gold nanoribbons

Gobind Basnet,[1] Krishna R. Panta,[1] Prem S. Thapa,[2] and Bret N. Flanders[1,a)]
[1]Department of Physics, Kansas State University, Manhattan, Kansas 66506, USA
[2]Imaging and Analytical Microscopy Laboratory, University of Kansas, Lawrence, Kansas 66045, USA

(Received 28 July 2016; accepted 28 January 2017; published online 14 February 2017)

This paper describes the electrochemical growth of branchless gold nanoribbons with ~40 nm × ~300 nm cross sections and >100 μm lengths (giving length-to-thickness aspect ratios of $>10^3$). These structures are useful for opto-electronic studies and as nanoscale electrodes. The 0.75–1.0 V voltage amplitude range is optimal for branchless ribbon growth. Reduced amplitudes induce no growth, possibly due to reversible redox chemistry of gold at reduced amplitudes, whereas elevated amplitudes, or excess electrical noise, induce significant side-branching. The inter-relatedness of voltage-amplitude, noise, and side-branching in electrochemical nanoribbon growth is demonstrated. *Published by AIP Publishing*. [http://dx.doi.org/10.1063/1.4976027]

Ultra-long nanowires and nanoribbons with aspect ratios $>10^3$ are useful samples for learning about fundamental opto-electronic processes, including ballistic and collective charge-transport on ultrafast time-scales.[1–3] Such studies will benefit from monolithic wires long enough to allow the excitation to propagate between spatially separated pump- and probe-illumination sites. In the physiology-venue, branchless nanowires are promising neural[4] and cellular probes.[5] *Directed electrochemical nanowire assembly* (DENA)[6] is a method for fabricating electrode-nanowire assemblies where the nanowire is a single crystal[7] of tunable diameter[8] and variable composition: In,[7] Au,[9] Cu,[10] Pt,[11] and Pd.[12] Growth is caused by applying an alternating voltage across working and counter electrodes (CEs) that are immersed in a salt solution, stimulating the dendritic crystallization of the metallic species at the (sharper) working electrode (WE) during the negative half cycles.[13] As the term *dendritic crystallization* suggests, the method tends to produce branched, TV-antenna-shaped structures, and one would like to control the degree to which side-branching occurs during the growth process. Prior applications of DENA have employed voltage-amplitudes of 4–8 V for Au,[9,14] Cu,[10] Pt, and Pd wires,[11,12] and ~16 V for In wires.[7] These values are several times larger than the standard reduction potentials of the metals. Here we have employed electro-etched working electrodes having <50 nm tip radii in order to realize growth at considerably lower amplitudes: 0.75–1.5 V. These factors enable the growth of *ultra-long* gold nanoribbons with length-to-thickness aspect ratios $>10^3$. A stability analysis illustrates how small voltages and minimal noise suppress the Mullins-Sekerka instability, rendering side-branching unlikely.

Figure 1(a) depicts the set-up for the DENA-based growth of gold nanoribbons.[6,9] This apparatus is mounted on the stage of an inverted microscope (Leica, IRB) under ambient conditions and consists of an electrode pair immersed in aqueous $KAuCl_4$ solution. To confine the growth to its tip, the working electrode (WE) must be sharper than the counter electrode (CE). Hence, we fabricate the WE by electro-etching 200 μm diameter gold wire (Ted Pella) until its foremost radius is <50 nm.[15] The scanning electron micrograph in Figure 1(b) and the inset show a typical WE with a ~25 nm tip radius. The comparatively blunt CE (not shown), made from 500 μm diameter gold wire (Kurt J. Lesker), is electro-etched to a ~2.5 μm radius. The CE is taped to a glass microscope slide that is mounted on the inverted microscope. The WE is mounted in a 3D stage and positioned to have ~1 μm inter-electrode gap relative to the CE. A ~20 μl aliquot of solution composed of aqueous 40.0 mM $KAuCl_4$ (Sigma) is deposited across the inter-electrode gap. Nanoribbon crystallization is induced by using a function generator (Hewlett Packard, 8116A) to apply a 10–50 MHz square-wave voltage signal to the WE, while grounding the CE. The profile in Figure 1(c) is a representative 37.0 MHz voltage signal. A small (~+35 mV) DC offset is also applied to prevent coating of the ribbon by polycrystalline gold. A component of this study requires the addition of a white-noise signal, supplied by a second function generator (Agilent, 33220A), to the square wave signal. A high bandwidth (4.0 GHz) summing amplifier is used to do so. The average growth velocity $\langle v \rangle$ of a nanoribbon is determined by collecting movies of its growth and computing the ratio $\Delta L/\Delta t$, where ΔL is the change in length and Δt the elapsed time. The surface of the microscope slide is made hydrophobic by coating it with poly-dimethyl silane (e.g., Rain-X), causing the solution drop to form a ~90° contact angle that permits the electrode-ribbon assembly to be pulled perpendicularly through the air-water interface—avoiding damaging lateral forces during extraction.

The cyclic voltammogram (CV) in Figure 1(d) illustrates the near-equilibrium redox behavior of gold. This CV plots the electronic current I into the WE versus the overpotential η of the WE. A positive current indicates a positive charge flow into the WE. The overall redox reaction is

$$Au^{III}Cl_4^-(aq) + 3e^- \leftrightarrow Au^{(0)} + 4Cl^-. \quad (1)$$

The overpotential is defined as $\eta = V_{App} - V_{Eq}$ where V_{App} is the applied potential, and V_{Eq} is the equilibrium potential at which no current flows. This CV was collected using essentially identical, gold working, reference, and counter-electrodes in 5.0 mM $KAuCl_4$ (aq) solution. Equation (1)

a)Author to whom correspondence should be addressed. Electronic mail: bret.flanders@phys.ksu.edu. Tel.: +1 785 532-1614.

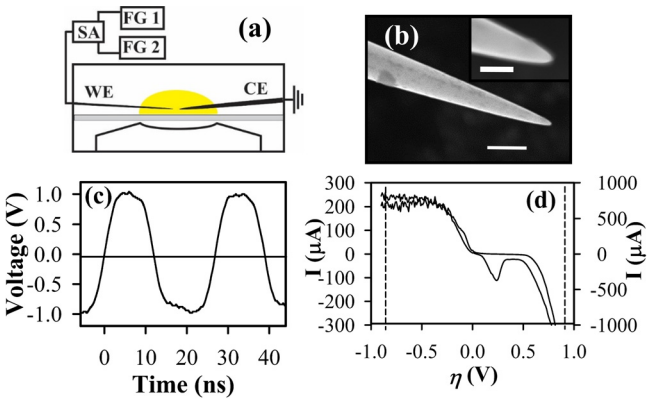

FIG. 1. (a) Side-view of experimental set-up. FG 1 and FG 2 denote the function generators; SA denotes a summing amplifier. (b) Scanning electron micrograph of a gold WE. Scale bar = 1.0 μm. *Inset:* enlarged view of tip. Scale bar = 200 nm. (c) Square-wave voltage signal used to grow gold nanoribbons. (d) Cyclic voltammogram of aqueous 5 mM $KAuCl_4$ solution, measured with gold WE, RE, and CE. Dashed lines indicate a typical square-wave amplitude in DENA. Scan rate = 10 mV/s.

runs forward (deposition) when a negative overpotential is applied and runs backwards (dissolution) when a positive overpotential is applied. The negative current drops sharply near +0.25 V, indicating that dissolution ceases.[16] This behavior is attributed to passivation of the WE interface.[16] More positive overpotential values have a little effect until water-oxidation begins near ~0.80 V. Hence, the redox electrochemistry of gold (Equation (1)) is asymmetric: negative overpotentials <-0.25 V induce deposition whereas positive overpotentials $>+0.25$ V do *not* induce comparable levels of dissolution.

Figure 2(a) is an optical micrograph of a gold ribbon that was grown by the DENA method with a 37.0 MHz square wave of amplitude 0.88 V. The ribbon is 261 μm long and branchless. A movie showing its growth is available online (Multimedia view). The 0.88 V amplitude used to grow this nanoribbon is indicated by the vertical dashed lines at ± 0.88 V in the CV of Figure 1(d). This comparison suggests that during DENA, the negative half cycle crystallizes gold whereas the positive half cycle has little effect (due to passivation[16]); hence, a full cycle causes net deposition. Some caution is warranted here as a conventional CV may not reflect the non-equilibrium behavior driven by a RF voltage. A scanning electron microscope (FEI Versa 3D Dual Beam) equipped with an energy dispersive X-ray spectrometer was used to characterize the $2.7 \times 2.7\ \mu m^2$ sample of a nanoribbon on ITO-coated glass, shown in the inset of Figure 2(a). Weight-percentages of 3.9% Au, 38.6% O, 30.3% Si, 6.2% Na, 10.3% In, and 3.0% Sn were observed, as well as trace quantities of Mg, K, Ca, and Al. The Au and O fluorescence maps [insets, Figure 2(a)] show that the Au signal correlates with the ribbon-location whereas the O signal anti-correlates with the ribbon-location, suggesting that the ribbon is composed of gold. The O, Si, Na, In, and Sn content are attributed to the substrate.

The ribbon-like nature of these nanostructures is evident in the scanning electron micrographs in Figures 2(b)–2(d). The widths of these (and 8 other) samples are between 130 nm and 360 nm. The tip-region shown in Figure 2(e) is narrower, having a lengthwise averaged diameter of 58 $\pm$ 3 nm, and the foremost tip width is ~10 nm (inset). The thickness of these ribbon-like wires was characterized by atomic force microscopy (Veeco, di Innova). Figure 2(f) is a topographical image of a 171 μm gold nanoribbon on a glass coverslip. (This image is a composite 8 overlapping images of the wire). Figure 2(g) compares the topographical profile of the spine of the ribbon to that of the adjacent glass substrate. The dashed line in panel (f) indicates the location of these profiles. The difference between their lengthwise averaged heights is 37 ± 9 nm, a value that is representative of the ribbon-thickness elsewhere along the structure. Hence, the length-to-thickness aspect ratio is 171 μm/37 nm $\approx 4.6 \times 10^3$ for this ribbon. We have topographically examined two other nanoribbons, obtaining the average thicknesses of 44 nm, and 39 nm, demonstrating that the growth of nanoribbons with high length-to-thickness aspect ratios is feasible with this technique.

Figure 3(a) depicts an electron diffraction pattern collected from the nanoribbon shown in panel (f). This study used a 200 kV electron microscope (FEI Tecnai F20 XT) that was set to a 290 mm camera length and a 10 μm diameter area selection aperture. Figure 3(b) shows the simulated

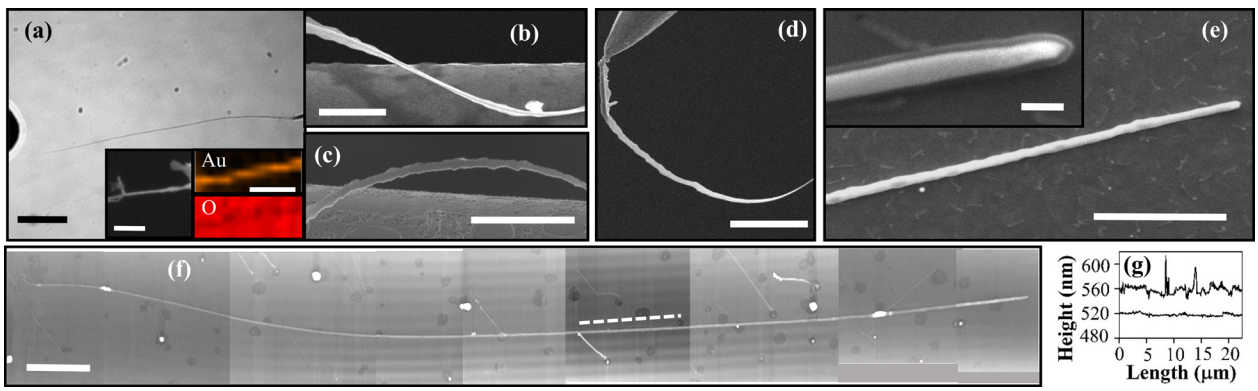

FIG. 2. (a) Optical image of a gold nanoribbon grown with a voltage amplitude of 0.88 V for 304 s. Scale bar = 50 μm. A video of this event is available online. Inset: SEM micrograph of a nanoribbon (left panel, Scale bar = 1 μm) and X-ray fluorescence maps of same segment showing locations of Au and O (as labeled, Scale bar = 500 nm). (b)–(d) Scanning electron micrographs of curved nanoribbon segments, displaying their ribbon-like shape. Scale bars = 1 μm, 2 μm, and 2 μm, respectively. (e) Scanning electron micrograph of tip region of nanoribbon. Scale bar = 1 μm. Inset: Enlarged view of tip region. Scale bar = 100 nm. (f) Composite topographical image of a ~171 μm long gold nanoribbon. Scale bar = 10 μm. (g) Height profiles collected from the spine of the nanoribbon and the adjacent substrate near the region indicated by the white dashed line in panel (f). (Multimedia view) [URL: http://dx.doi.org/10.1063/1.4976027.1]

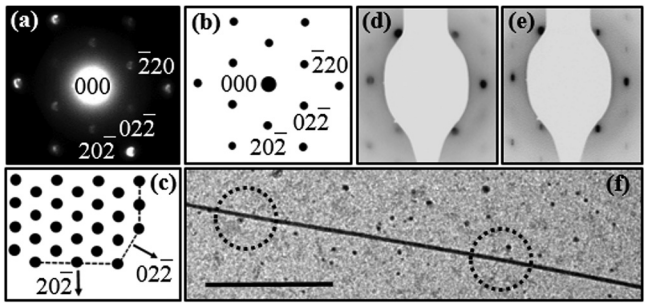

FIG. 3. (a) Selected area electron diffraction pattern of the nanoribbon shown in panel (f). (b) Simulated electron diffraction pattern of single crystalline gold viewed along the [111] zone axis. (c) Real space schematic corresponding to the pattern shown in panel (a). (d) and (e) Diffraction patterns collected from the nanoribbon-regions marked by the circles in panel (f). (f) Transmission electron micrograph of a gold nanoribbon. Scale bar = 20 μm.

pattern (calculated with CSpot 1.2.0) for face centered cubic gold ($Fm\bar{3}m$ space group) with lattice parameters of $a = b = c = 0.40786$ nm, viewed along the [111] zone axis.[17] The measured and simulated patterns are in excellent agreement, confirming the gold composition of the ribbon. Figure 3(c) is an atomic-level schematic of the (111) surface, corresponding to the orientation in panel (a). Figures 3(d) and 3(e) depict the selected area electron diffraction patterns that were collected from the sites indicated by the circles in panel (f). (A beam stop blocks the 000 spot and the first ring of spots in these patterns). The six spots in both of the patterns are identically oriented. The invariant positions of the spots indicate that the crystal structure of this nanoribbon does not change along the 46 μm length that was examined in this study. A similar result was observed with electrochemically grown gold nanowires.[9]

Ribbon growth is difficult to induce with voltage amplitudes less than 0.750 V whereas larger amplitudes not only cause increasingly rapid growth but also enhance the likelihood of side-branching. Samples grown at the same frequency (37.0 MHz) but with amplitudes ranging from 1.05 V to 1.5 V are shown in Figures 4(a)–4(c), respectively. The degree of side-branching increases significantly across this range. The distances between adjacent branches in panels (a)–(c) lie in the 1.1 to 8.2 μm range. Thermal noise is a commonly cited cause of side-branching in the dendritic crystallization of super-cooled melts.[18–20] To see if electrical noise induces side-branching in electrochemical dendritic growth, we have used a summing amplifier to add 800 mV of 20 MHz bandwidth-limited white noise to the 37.0 MHz square wave that was used to drive nanoribbon growth. The inset to Figure 4(d) shows the 1.0 V square wave (dashed line), the 800 mV white-noise (dotted line), and the combined signal (solid line). Figure 4(d) shows a nanoribbon that was grown using the square wave alone. The noise component was then added. Figure 4(e) was collected ~20 s later, showing the branched structure that developed in response to the added noise. The arrow indicates the tip position when the noise was added. A movie depicting the growth of this structure is available online (Multimedia view). A null effect was observed when only noise (up to 1.7 V) and no square wave signal was applied. These data show that excess electrical noise induces side-branching, and, consequently, can

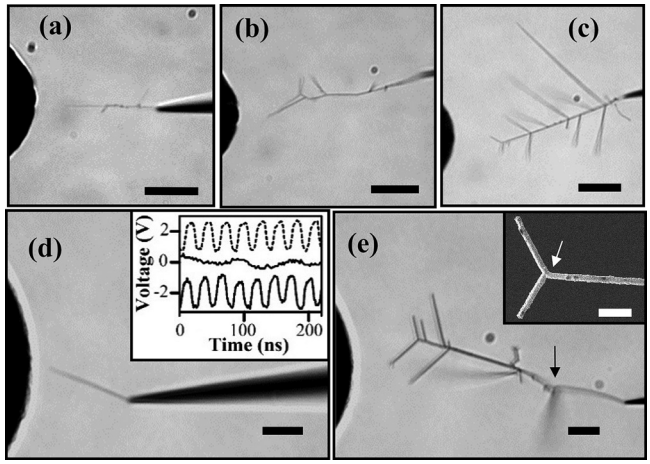

FIG. 4. (a) Optical images of gold dendrites grown with amplitudes of (a) 1.05 V for 79 s; (b) 1.2 V for 59 s; and (c) 1.5 V for 16 s. Scale bars = 20 μm. (d) Optical image of a gold nanoribbon grown with a square wave, as for Figure 2(a). Scale bar = 10 μm. *Inset*: 37.0 MHz square wave (dashed line), noise (middle solid line), and combined (lower solid line) voltage signals. Vertical offsets were added to separate the profiles. (e) Optical image of the nanoribbon after application of the *square wave + noise* signals. The arrow denotes the point at which the noise was turned on. Scale bar = 10 μm. A video of this event is available online. Inset: Y-shaped structure grown by applying a noise pulse. Scale bar = 2 μm. (Multimedia view) [URL: http://dx.doi.org/10.1063/1.4976027.2]

be used to tailor the morphology. For example, the Y-shaped structure in the inset, of potential interest for studying surface plasmon-propagation through a junction, was grown by applying a ~4 s pulse of noise at the designated point.

Direct measurement of the current during the (13.5 ns) negative half-cycles is challenging as only a few atoms join the crystal during this period. Instead, we have estimated the current density associated with deposition (i.e., the Faradic current density) by observing the nanoribbon growth velocity. Figure 5(a) plots the average growth velocity $\langle v \rangle$ (unfilled circles) versus the voltage amplitude. Mass conservation implies that growth at velocity $\langle v \rangle$ requires an average current density of

$$\langle j \rangle \cong ze\rho_{Au}\langle v \rangle, \tag{2}$$

where $\rho_{Au} = 5.89 \times 10^{28}\,\mathrm{m}^{-3}$ is the number density of gold, and ze (where $z = 3$) is the charge that is transferred during a step of Equation (1). These values (filled circles) are given by the right axis in Figure 5(a). The current density increases

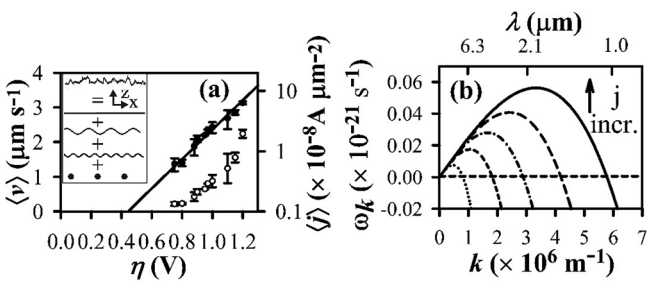

FIG. 5. (a) Growth speed (unfilled circles) and Faradic current density (filled circles) versus the amplitude of the alternating voltage signal. *Fit parameters:* $T = 300$ K; $c_O = 0.6 \times c_O^*$; $c_O^* = 40$ mM $= 2.41 \times 10^{25}\,\mathrm{m}^{-3}$; $\rho_M = 5.89 \times 10^{28}\,\mathrm{m}^{-3}$; $\gamma = 100\,\mathrm{J\ m}^{-2}$; $\kappa = (30 \times 10^{-9}\ \mathrm{m})^{-1}$. *Inset:* schematic of a rough interface decomposed into its Fourier modes. (b) Amplification rate versus wave vector for five arbitrarily chosen j-values.

sharply with amplitude beyond a threshold of ~750 mV. This plot is essentially a *non-equilibrium* voltammogram for gold reduction during DENA. To model this process, we assume that the overall deposition process (Equation (1)) is rate-limited by a single-electron step of the form $O^z + e^- = R^0$, where O^z is a gold species in the $z = 1$ oxidation state, and R^0 is the rate-limited product. The Butler-Volmer equation relates the current density collected by an electrode to the overpotential η[21]

$$j = j_0 \left[\frac{c_O}{c_O^*} e^{-\alpha\beta\left(e\eta - \frac{1}{\beta} ln\frac{c_O}{c_O^*} + \rho_{Au}^{-1}\gamma\kappa\right)} - e^{(1-\alpha)\beta\left(e\eta - \frac{1}{\beta} ln\frac{c_O}{c_O^*} + \rho_{Au}^{-1}\gamma\kappa\right)} \right], \tag{3}$$

where η is defined above. α is the symmetry factor associated with the energy barrier to reduction, and β is the inverse thermal energy $(k_B T)^{-1}$. c_O (c_O*) is the interfacial (bulk) concentration of species O^z. The Gibbs-Thomson factor $\rho_{Au}^{-1}\gamma\kappa$ accounts for curvature effects:[22] γ is the surface tension of the gold-solution interface, and κ is the local curvature of the interface defined such that a protrusion (depression) has a positive (negative) curvature. The solid line in Figure 5(a) is a best-fit of Equation (3) to the estimated current density data. An exchange current density of $j_0 \sim 1100\,\mathrm{A\,m^{-2}}$ and symmetry factor $\alpha = 0.145$ are needed to account for the ~750 mV threshold to charge flow. The other fitting parameter-values are reported in the caption. The fit-quality is reasonably good, indicating that the Butler-Volmer model accurately describes the high frequency (37 MHz) gold reduction that occurs during the DENA process.

A linear stability analysis by Haataja and co-workers illustrates how electrochemical systems that obey Equation (3) can become unstable and undergo side-branching.[21] A microscopically rough interface is sketched in the inset to Figure 5(a). Let this interface represent a profile of the nanoribbon, like that in Figure 2(g). This profile $z(x,t)$ may be decomposed into a sum of Fourier modes, each of spatial frequency k (units: rad/m), a few of which are sketched in the inset. The contribution of a single mode is $z + \delta z_k(x,t) = vt + \delta z_{0,k} e^{ikx} e^{\omega_k t}$. v is the steady-state growth velocity of the interface in the z-direction, and $\delta z_{0,k}$ is the amplitude of the kth mode. The factor $e^{\omega_k t}$ is the stability factor. If the surface is stable, the amplification rate ω_k (for each mode) is equal to zero, but for an unstable surface ω_k is non-zero. If ω_k is positive (negative), mode k will experience amplified (retarded) growth. If, for example, all modes other than k are stable, the nanoribbon-profile will become wave-like (with spatial wavelength $\lambda = 2\pi/k$), and the crests of the wave will become side-branches. This effect occurs because a protrusion on a surface steepens the local solute concentration gradient and, thereby, increases the local current density and the growth rate of the protrusion. This feedback mechanism is known as the Mullins-Sekerka instability.[23] Time-differentiation of $z + \delta z_k$ gives the growth velocity of the kth mode: $v + \delta v_k = v + \omega_k \delta z_k$. Growth at velocity $v + \delta v_k$ requires a current density $j + \delta j_k \cong ne\rho_{Au}(v + \delta v_k)$, where Equation (2) was used. Substituting $\omega_k \delta z_k$ for δv_k gives the current density fluctuation, which is a measure of the electrical noise level

$$\delta j_k(x,t) = ne\omega_k \rho_{Au} \delta z_k. \tag{4}$$

Hence, the noise-level δj_k and the amplification rate ω_k are proportional to each other, implying that elevated noise levels can amplify the growth rate of the protrusions.

For a roughened but flat electrochemical interface, Haataja and co-workers[21] have derived a dispersion relation for ω_k: (Equation 16 in Ref. 21)

$$\omega_k \cong \frac{\bar{j}k\left[\bar{j}(1+\alpha) - \left(\frac{3}{2} - \bar{j}\right)\hat{\gamma}\alpha k^2\right]}{\rho_{Au}\left[\bar{j}(1+\alpha) + \left(\frac{3}{2} - \bar{j}\right)k\right]}, \tag{5}$$

where the unitless current density is $\bar{j} = \frac{j}{j_O}$ and $j_O = \frac{neDc_O^*}{L_\infty}$. This function is plotted for five experimentally realized j-values (near $4.9 \times 10^{-8}\,\mathrm{A\,\mu m^{-2}}$) in Figure 5(b). To attain these plots, the diffusion coefficient of gold chloride was estimated to be $D \sim 1.0 \times 10^{-9}\,\mathrm{m^2\,s^{-1}}$, and a value of $L_\infty = 3.5 \times 10^{-6}\,\mathrm{m}$ was used for the diffusion length, giving $j_O \cong 3306\,\mathrm{A\,m^{-2}}$. These plots show that ω_k is positive for finite ranges of k-values, denoting the unstable modes. Moreover, the magnitude of ω_k across these unstable regions increases with j. Hence, larger voltage amplitudes V_{App}, which drive larger current densities j [by Equation (3)], are expected to induce stronger degrees of side-branching. Thus, an upsurge in either the amplitude V_{App} or the noise δj_k will inflate the amplification rate ω_k and induce side-branching. This picture explains our main observations: that minimal voltage amplitudes are required to suppress side-branching, and that excess noise tends to induce it (Figure 4). A more quantitative analysis will benefit from direct measurement of the deposition current density and a 3D theory that addresses the cylindrical geometry and, possibly, surface tension anisotropy of the crystalline nanoribbon.

In conclusion, we report the methodology for the electrochemical growth of ultra-long, branchless gold nanoribbons. Their fabrication is enabled by the use of sharp, electro-etched working electrodes that permit wire growth with voltage amplitudes in the 0.75–1.0 V range. Reduced amplitudes induce no growth, possibly due to the nearly reversible redox chemistry of gold at low amplitudes, whereas elevated amplitudes, or excess electrical noise, strongly enhance the degree-of side-branching. Collectively, these results illuminate the relationship between voltage amplitude, electrical noise, and side-branch formation during electrochemical dendritic growth and illustrate how side-branching may be controlled. The fabrication of long, branchless nanoribbons is one application. It is also possible to add noise in a controlled manner in order to fabricate nanoribbons with branches at selected points along the main trunk—another structure of optoelectronic interest. Finally, the common effect (side-branch formation) that amplitude and noise cause suggests that *shot noise*, which scales with amplitude, may be an important factor in the DENA process. This possibility will be examined in the future.

This work was supported by an NSF EPSCoR IRR Track II Nebraska-Kansas Collaborative Research Award (1430519) and the NIH Brain Initiative (1R21EY026392).

We thank Professor Larry Weaver for edifying theoretical insights and Tim Sobering and David Thurmstrom for electronic assistance.

[1]B. Wild, J. Cao, Y. Sun, B. P. Khanal, E. R. Zubarev, S. K. Gray, N. F. Scherer, and M. Pelton, ACS Nano **6**(1), 472–482 (2012).
[2]A. M. Summers, A. S. Ramm, G. Paneru, M. F. Kling, B. N. Flanders, and C. A. Trallero-Herrero, Opt. Express **22**(4), 4235–4246 (2014).
[3]Z. Fan, M. Bosman, X. Huang, D. Huang, Y. Yu, K. P. Ong, Y. A. Akimov, L. Wu, B. Li, J. Wu, Y. Huang, Q. Liu, C. E. Png, C. L. Gan, P. Yang, and H. Zhang, Nat. Commun. **6**, 7684 (2015).
[4]M. Kang, S. Jung, H. Zhang, T. Kang, H. Kang, Y. Yoo, J.-P. Hong, J.-P. Ahn, J. Kwak, D. Jeon, N. A. Kotov, and B. Kim, ACS Nano **8**(8), 8182–8189 (2014).
[5]G. Paneru, P. S. Thapa, S. P. Mcbride, A. Ramm, B. M. Law, and B. N. Flanders, Nanotechnology **23**, 455105 (2012).
[6]B. N. Flanders, Mod. Phys. Lett. B **26**(1), 1130001 (2012).
[7]I. Talukdar, B. Ozturk, T. D. Mishima, and B. N. Flanders, Appl. Phys. Lett. **88**, 221907 (2006).
[8]B. Ozturk, I. Talukdar, and B. N. Flanders, Nanotechnology **18**, 365302 (2007).
[9]B. Ozturk, T. Mishima, D. R. Grischkowsky, and B. N. Flanders, Nanotechnology **18**, 175707 (2007).
[10]C. Schmädicke, M. Poetschke, L. D. Renner, L. Baraban, M. Bobetha, and G. Cuniberti, RSC Adv. **4**, 46363–46368 (2014).
[11]J. K. Kawasaki and C. B. Arnold, Nano Lett. **11**, 781–785 (2011).
[12]C. Cheng, R. K. Gonela, Q. Gu, and D. T. Haynie, Nano Lett. **5**(1), 175–178 (2005).
[13]M. A. Diaz, G. H. Kelsall, and N. J. Welham, J. Electroanal. Chem. **361**(1–2), 25–38 (1993).
[14]G. Paneru and B. N. Flanders, Nanoscale **6**(2), 833–841 (2014).
[15]Y. Qiao, J. Chen, X. Guo, D. Cantrell, R. Ruoff, and J. Troy, Nanotechnology **16**, 1598–1602 (2005).
[16]J. Herrera-Gallego, C. E. Castellano, A. J. Calandra, and A. J. Arvia, J. Electroanal. Chem. Inter. Electrochem. **66**(3), 207–230 (1975).
[17]H. E. Swanson, R. K. Fuyat, and G. M. Ugrinic, Natl. Bur. Stand. Circ. **539 3**, 3 (1954), available at http://hdl.handle.net/2027/mdp.39015077578519.
[18]J. S. Langer, Phys. Rev. A **36**(7), 3350–3358 (1987).
[19]E. Brener and D. Temkin, Phys. Rev. E **51**(1), 351–359 (1995).
[20]U. Bisang and J. H. Bilgram, Phys. Rev. Lett. **75**(21), 3898–3901 (1995).
[21]M. Haataja, D. J. Srolovitz, and A. B. Bocarsly, J. Electrochem. Soc. **150**(10), C699–C707 (2003).
[22]J. S. Langer, Rev. Mod. Phys. **52**(1), 1–28 (1980).
[23]W. W. Mullins and R. F. Sekerka, J. Appl. Phys. **34**(2), 323–329 (1963).